Nanoscale Advances

ROYAL SOCIETY OF CHEMISTRY

PAPER

View Article Online
View Journal | View Issue

Cite this: *Nanoscale Adv.*, 2024, **6**, 4128

Large piezoelectric responses and ultra-high carrier mobility in Janus $HfGeZ_3H$ (Z = N, P, As) monolayers: a first-principles study

Tuan V. Vu, [ab] Huynh V. Phuc, [*c] Le T. T. Phuong, [d] Vo T. T. Vi, [e] A. I. Kartamyshev[ab] and Nguyen N. Hieu [*fg]

Breaking structural symmetry in two-dimensional layered Janus materials can result in enhanced new phenomena and create additional degrees of piezoelectric responses. In this study, we theoretically design a series of Janus monolayers $HfGeZ_3H$ (Z = N, P, As) and investigate their structural characteristics, crystal stability, piezoelectric responses, electronic features, and carrier mobility using first-principles calculations. Phonon dispersion analysis confirms that $HfGeZ_3H$ monolayers are dynamically stable and their mechanical stability is also confirmed through the Born–Huang criteria. It is demonstrated that while $HfGeN_3H$ is a semiconductor with a large bandgap of 3.50 eV, $HfGeP_3H$ and $HfGeAs_3H$ monolayers have narrower bandgaps being 1.07 and 0.92 eV, respectively. When the spin–orbit coupling is included, large spin-splitting energy is found in the electronic bands of $HfGeZ_3H$. Janus $HfGeZ_3H$ monolayers can be treated as piezoelectric semiconductors with the coexistence of both in-plane and out-of-plane piezoelectric responses. In particular, $HfGeZ_3H$ monolayers exhibit ultra-high electron mobilities up to 6.40 × 10^3 cm^2 V^{-1} s^{-1} ($HfGeAs_3H$), indicating that they have potential for various applications in nanoelectronics.

Received 11th April 2024
Accepted 13th June 2024

DOI: 10.1039/d4na00304g

rsc.li/nanoscale-advances

1 Introduction

The piezoelectric property of materials demonstrates the ability to convert energy effectively from electrical to mechanical energy and *vice versa*. This property is attracting the attention of scientists due to its applications in various fields, such as sensors, nanogenerators, and medical devices.[1–3] The correlation between piezoelectricity and the symmetry of the crystal structure is widely recognized.[4] A material is classified as piezoelectric when it possesses a non-centrosymmetric crystal structure. Recent studies have shown that 2D nanomaterials have great potential for application in piezoelectric devices because they possess strong piezoelectric effects.[5,6]

In parallel with the search for new 2D structures, scientists have succeeded in creating asymmetric Janus structures based on known symmetric 2D structures, *i.e.* successfully synthesizing Janus MoSSe sheets.[7,8] The successful fabrication of 2D Janus materials has provided us with a new approach to studying 2D structures. As a consequence, many Janus structures have been proposed and studied systematically.[9–12] Due to the lack of vertical symmetry, Janus structures possess many outstanding physical characteristics compared to their original symmetric structures.[13–16] Janus materials show diverse application prospects in various fields, such as electronics, optoelectronics, thermoelectrics, and water-splitting catalysts.[17–20] In particular, 2D Janus materials exhibit adherence to the non-centrosymmetric requirement, hence demonstrating their potential as piezoelectric materials.[21–24] The piezoelectric effect was predicted in the MoS_2 monolayer[6] and was later confirmed experimentally.[25,26] Group IV monochalcogenides have shown strong piezoelectric responses with a piezoelectric coefficient of 251 pm V^{-1}.[27] The piezoelectric effect has also been found in Janus group III chalcogenide monolayers with an in-plane piezoelectric coefficient of up to 8.47 pm V^{-1}.[28] Besides, the reduction of mirror symmetry in the Janus structure gives rise to vertical polarization, leading to enhanced out-of-plane piezoelectricity.[28] Very recently, the piezoelectric effect has been reported in other 2D Janus materials, such as γ-Sn_2XY (X/Y = S, Se, Te)[29] or $WSiZ_3H$ (Z = N, P, As).[30]

Very recently, a $MoSi_2N_4$ sheet was successfully experimentally fabricated,[31] paving the way for a new 2D family, called the MA_2Z_4

[a]*Laboratory for Computational Physics, Institute for Computational Science and Artificial Intelligence, Van Lang University, Ho Chi Minh City, Vietnam. E-mail: tuan.vu@vlu.edu.vn*

[b]*Faculty of Mechanical – Electrical and Computer Engineering, School of Technology, Van Lang University, Ho Chi Minh City, Vietnam*

[c]*Division of Physics, School of Education, Dong Thap University, Cao Lanh 870000, Vietnam. E-mail: hvphuc@dthu.edu.vn*

[d]*Department of Physics, University of Education, Hue Unversity, Hue, Vietnam*

[e]*Faculty of Basic Sciences, University of Medicine and Pharmacy, Hue University, Hue, Vietnam*

[f]*Institute of Research and Development, Duy Tan University, Da Nang 550000, Vietnam. E-mail: hieunn@duytan.edu.vn*

[g]*Faculty of Natural Sciences, Duy Tan University, Da Nang 550000, Vietnam*

family,[32] with many interesting application prospects. Soon after, many MA_2Z_4-based Janus structures were proposed, including $XMoSiN_2$ (X = S, Se, Te)[33] and $MGeSiP_4$ (M = Ti, Zr, Hf).[34] Many novel physical properties have been reported in MA_2Z_4-based Janus materials.[35–37] In this study, we propose the 2D Janus $HfGeZ_3H$ (Z = N, P, As) monolayers and systematically investigate their crystal structure characteristics, electronic states, elasticity, and piezoelectric responses as well as the mobility of carriers.

2 Calculation details

The Vienna *ab initio* simulation package[38,39] was utilized to perform first-principles calculations based on the projector augmented wave approach.[40,41] The electron exchange–correlation functional was treated using the generalized gradient approximation parameterized using the Perdew, Burke, and Ernzerhof (PBE) functional.[42] The hybrid functional suggested by Heyd, Scuseria, and Ernzerhof (HSE06) was employed to enhance the precision of electronic band gap analysis.[43] The semiempirical DFT-D3 technique was applied for the weak van der Waals forces, which may be available in the layered material.[44] Spin–orbit coupling (SOC) was incorporated into the self-consistent computations in order to examine the consequences of SOC.[45] The plane wave basis set's energy cutoff was set at 650 eV and a $12 \times 12 \times 1$ *k*-point mesh grid was used to sample the Brillouin zone integration. Atom positions in the crystal were totally relaxed until the forces on each atom were lower than 1×10^{-3} eV Å^{-1}. The energy convergence threshold was chosen to be 1×10^{-6} eV. A 35 Å vacuum space was inserted into the vertical axis to reduce the interlayer interactions. We used the frozen-phonon technique as performed using the PHONOPY code to compute the phonon spectra.[46] The thermal stability of the investigated structures was examined *via ab initio* molecular dynamics (AIMD) simulations at a constant temperature of 300 K with a canonical ensemble within 10 ps (time step of 1 fs). To rectify the dipole moment built in the asymmetric material, we added the dipole correction to our calculation. The elasticity and piezoelectricity were investigated using the strain–stress relationships and density functional perturbation theory (DFPT). The deformation potential technique was employed in order to examine carrier mobility in the studied structures.[47]

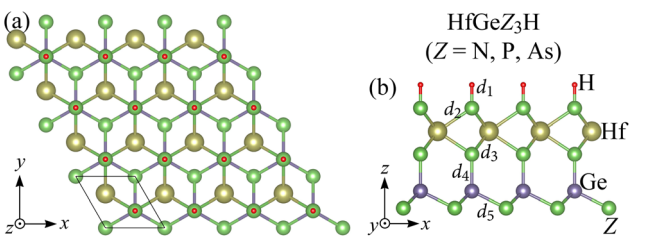

Fig. 1 Crystal structures of Janus $HfGeZ_3H$ (Z = N, P, As) monolayers in the (a) top and (b) side views.

3 Results and discussion

3.1 Crystal structure and stability

The optimized crystal structure of the Janus $HfGeZ_3H$ (Z = N, P, As) monolayers is shown in Fig. 1. The unit cell of Janus $HfGeZ_3H$, as denoted by the rhombus in Fig. 1(a), consists of six atoms, including three Z atoms, one H atom, one Hf atom, and one Ge atom. It is calculated that the lattice parameter *a* of $HfGeZ_3H$ is from 3.16 to 3.88 Å, which depends on the atomic size of the Z element. Due to the small atomic size of N compared with P and As the values of the structural parameters of $HfGeN_3H$ are much lower than those of $HfGeP_3H$ and $HfGeAs_3H$ as revealed in Table 1. The lattice parameters for the Janus $HfGeZ_3H$ monolayers are comparable to those of $HfGe_2Z_4$.[32]

To evaluate the possibility of Janus $HfGeZ_3H$ monolayers being fabricated experimentally, we investigated their stability by calculating their phonon dispersion and cohesive energies. Fig. 2(a) presents the phonon spectra of all examined compounds. It is indicated that there are 18 vibrational branches in the Brillouin zone due to the presence of six atoms in the unit cell. As shown in Fig. 2(a), there are certain frequency ranges where the optical modes and acoustic modes coexist, which could result in strong acoustic-optical scattering in the studied structures. Besides, we can observe a large distinct phononic gap in the optical region in the phonon dispersion of Janus $HfGeZ_3H$ monolayers. This is due to the large difference in mass between the constituent elements in the examined compounds. Notably, the vibrational branches all contain real frequencies in the whole first Brillouin zone, reflecting the dynamically stable structure of these Janus monolayers. Furthermore, we performed AIMD simulations to verify the thermal stability of the examined structures at room temperature. The calculated results for the variations in the temperature during AIMD simulation of $HfGeZ_3H$ monolayers are revealed in Fig. 2(b). It is indicated that the temperature fluctuations are small at around 300 K and the crystal structures of $HfGeZ_3H$ remain robust throughout the 10 ps of AIMD simulation. There is neither chemical bond breaking nor structural phase transition during AIMD simulation. These support the hypothesis that the $HfGeZ_3H$ monolayers are thermally stable. Indeed, we explore the cohesive energy to examine the bond strength

Table 1 Lattice constant *a* (Å), thickness *h* (Å) bond length *d* (Å), cohesive energy E_{coh} (eV per atom), and Bader charger *q* (|*e*|) of atoms for Janus $HfGeZ_3H$ monolayers

	a	*h*	d_1	d_2	d_3	d_4	d_5	E_{coh}	q_{Hf}	q_{Ge}	q_{Z_1}	q_{Z_2}	q_{Z_3}	q_H
$HfGeN_3H$	3.16	5.88	1.02	2.18	2.19	1.87	1.91	−7.28	−1.933	−1.577	1.067	1.406	1.128	−0.092
$HfGeP_3H$	3.74	7.65	1.42	2.60	2.60	2.31	2.39	−6.47	−0.731	−0.010	−0.206	0.493	−0.051	0.506
$HfGeAs_3H$	3.88	8.05	1.53	2.70	2.69	2.42	2.50	−5.05	−0.631	−0.070	−0.306	0.555	−0.107	0.558

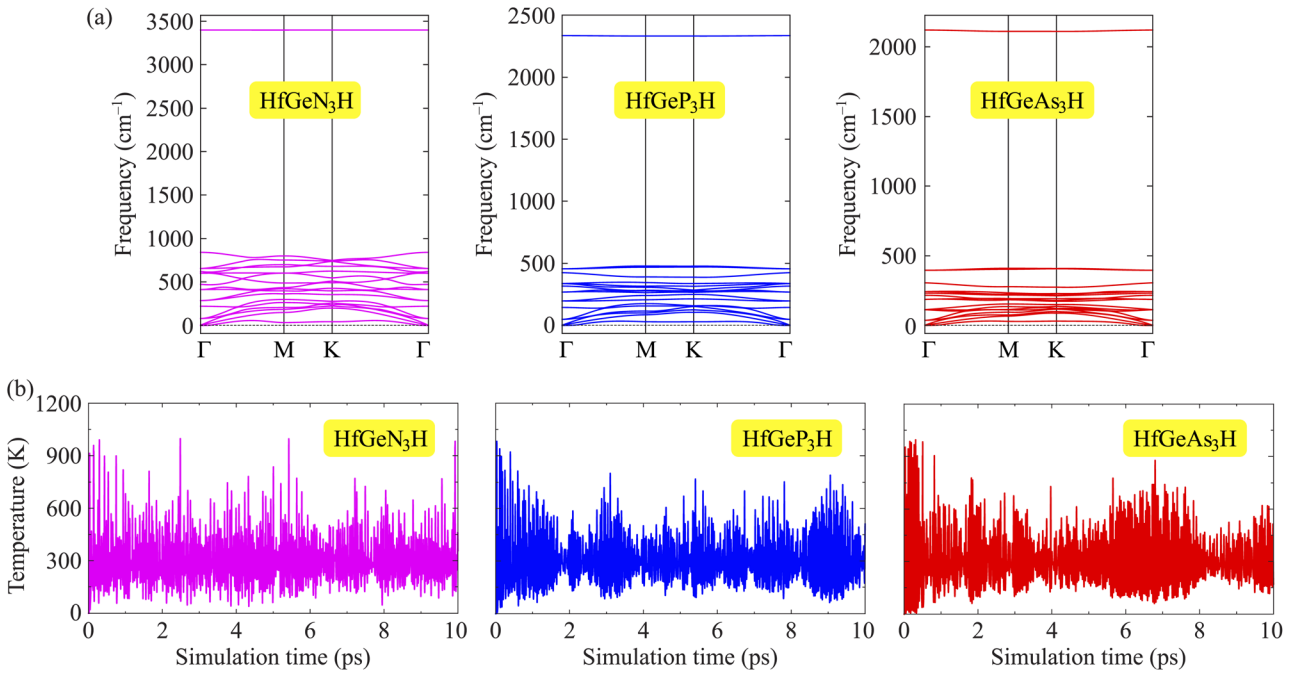

Fig. 2 Phonon dispersion (a) and variations of temperature during AIMD simulation at room temperature (b) of Janus $HfGeN_3H$, $HfGeP_3H$, and $HfGeAs_3H$ monolayers.

between atoms in the Janus configurations. Cohesive energy per atom is determined according to the following formula:

$$E_{coh} = \frac{E_{tot} - (E_{Hf} + E_{Ge} + 3E_Z + E_H)}{6}, \quad (1)$$

where E_{tot} denotes the total energy of Janus $HfGeZ_3H$; E_{Hf}, E_{Ge}, E_H, and E_Z are the energies of single atoms Hf, Ge, H, and Z, respectively.

Our computed results show that the cohesive energy, which is calculated using eqn (1), has a negative value, as presented in Table 1, confirming the energetic stability of the examined monolayers. The values of E_{coh} are calculated to be −7.28, −6.47, and −5.05 eV per atom for $HfGeN_3H$, $HfGeP_3H$, and $HfGeAs_3H$, respectively. Thus, the most energetically stable structure is $HfGeN_3H$. This is consistent with the fact that the shorter the chemical bonds, the stronger the bond. Furthermore, we also carry out a Bader charge analysis to get insight into the charge transfer between the atoms in the considered compounds. In Table 1, we report the computed results for the atomic Bader charges. It is easy to see that the H atom loses a small amount of charge in the 2D compound $HfGeN_3H$. For the other compounds, most of the effective electrons move to the H atom. Besides, we observe that the Hf and Ge atoms lose their charges.

3.2 Electronic characteristics

We here discover the intriguing electronic features of the 2D $HfGeZ_3H$ systems. We first explore the band structures of $HfGeZ_3H$ as presented in Fig. 3. It is demonstrated that while $HfGeN_3H$ is a wide direct bandgap semiconductor, both $HfGeP_3H$ and $HfGeAs_3H$ are semiconductors with narrower indirect bandgaps. The calculated values for the bandgap of $HfGeN_3H$, $HfGeP_3H$, and $HfGeAs_3H$ are 2.28, 0.41, and 0.29 eV, respectively. Although the PBE method is a popular method for predicting the electronic characteristics of materials, this method is known to underestimate the accuracy of bandgaps of

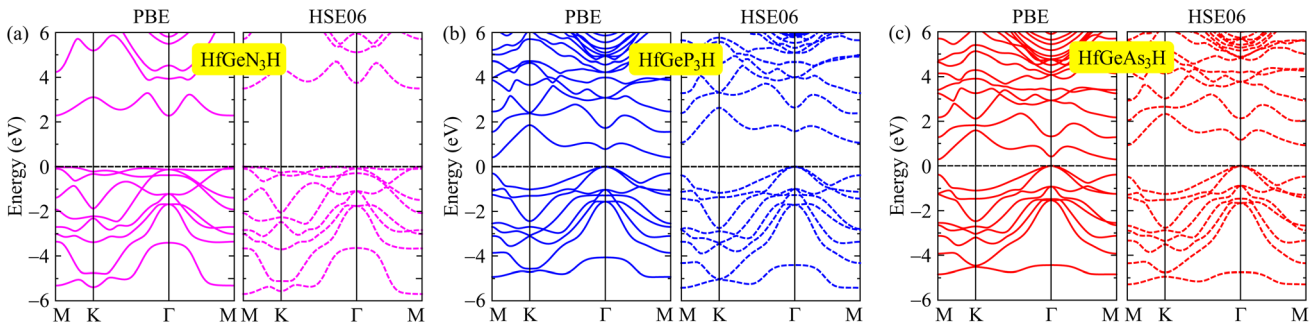

Fig. 3 Band structures of (a) $HfGeN_3H$, (b) $HfGeP_3H$, and (c) $HfGeAs_3H$ at the PBE and HSE06 theoretical levels.

Table 2 The PBE/HSE06/PBE + SOC bandgap E_g (eV), spin-splitting energy λ_c (eV), vacuum level difference $\Delta\Phi$ (eV), and work function Φ of $HfGeZ_3H$ monolayers

	E_g^{PBE}	E_g^{HSE06}	$E_g^{PBE+SOC}$	λ_c	$\Delta\varphi$	φ_H	φ_Z
$WSiN_3H$	2.28	3.50	2.21	0.30	2.66	3.36	6.02
$WSiP_3H$	0.41	1.07	0.36	0.26	0.68	2.70	3.38
$WSiAs_3H$	0.29	0.92	0.17	0.36	0.19	2.68	2.87

semiconductors and insulators as demonstrated by Perdew and Levy.[48] The GW approximation[49] or hybrid functionals, such as HSE06,[43] are considered a suitable solution for tuning the band diagrams of semiconductors. At the HSE06 theoretical level, the bandgaps of $HfGeN_3H$, $HfGeP_3H$, and $HfGeAs_3H$ are predicted to be 3.50, 1.07, and 0.92 eV, respectively. It is clear that due to the larger atomic radii of P and As compared to N, there is a reduced overlap of atomic orbitals in $HfGeP_3H$ and $HfGeAs_3H$, which results in their bandgaps being smaller than that of $HfGeN_3H$. By using the PBE functional, the computed bandgaps of $HfGeZ_3H$ are much narrower than those evaluated by the HSE06 approach. The computed data for the bandgaps of $HfGeZ_3H$ are presented in Table 2.

When compounds are formed from heavy elements, the SOC significantly influences their electronic characteristics. The electronic landscape of 2D layered materials is enhanced by the SOC effect, which renders them adaptable to a variety of applications ranging from traditional electronics to cutting-edge domains such as valleytronics and spintronics. The SOC can remove the degeneracy of electronic states, leading to energy splitting in the electronic bands, and can also modify the band gap of the studied structures. The strength of SOC in 2D structures can be tuned in different ways, including structural modifications, particularly in structures with a lack of inversion symmetry. Enhanced SOC in 2D structures could be useful for applications in spintronic devices, where the spin degree of freedom is a key parameter for spintronics. To evaluate the influences of the SOC on the electronic features of $HfGeZ_3H$, we determined their energy band structures using the PBE + SOC approach as depicted in Fig. 4. When the SOC is taken into account, spin degeneracy is eliminated and there is spin splitting in the band structure of the studied materials. It is shown that a large spin-splitting energy λ_c is found at the k point of the conduction band. The calculated value of λ_c for $HfGeN_3H$, $HfGeP_3H$, and $HfGeAs_3H$ is found to be 0.30, 0.26, and 0.36 eV respectively. In the presence of the SOC effect, the bandgap of $HfGeZ_3H$ is slightly reduced. The PBE + SOC bandgaps of $HfGeN_3H$, $HfGeP_3H$, and $HfGeAs_3H$ are respectively 2.21, 0.36, and 0.17 eV as revealed in Table 2.

In Fig. 5, we reveal the weighted bands of $HfGeZ_3H$ to better see the contribution of atomic orbitals in the formation of their electronic band structure. As depicted in Fig. 5, we can see that the tendency to form the band structure is similar in all investigated monolayers. It is indicated that the conduction band minimum (CBM) of $HfGeZ_3H$ monolayers is mainly contributed by the Hf-d orbitals. Meanwhile, the p orbitals of the group V elements (N, P, and As) play a major role in forming the valence band, particularly around the valence band maximum (VBM). The Hf-d orbitals also have a significant contribution to the valence band near the Fermi level.

One of the essential electronic properties that we need to investigate is the electrostatic potential and work function. The work function tells us about the ability of electrons to escape from the material, and it depends on the vacuum level E_v and Fermi level E_f as $\varphi = E_v - E_f$. Since Janus structures have a vertically asymmetric crystal structure with atomic layers of different electronegativities, polarization exists along the vertical direction. In other words, the lack of mirror symmetry causes an out-of-plane polarization in the Janus structure. It should also be noted that large differences in electronegativity between the surfaces will directly affect the value of the out-of-plane piezoelectric constants. Therefore, when evaluating the electrostatic potential of Janus materials, we need to include the dipole correction in the calculations for the electrostatic potential. Fig. 6 shows the electrostatic potential of the investigated monolayers with dipole corrections. It is easy to recognize the asymmetry in the shape of the electrostatic potential,

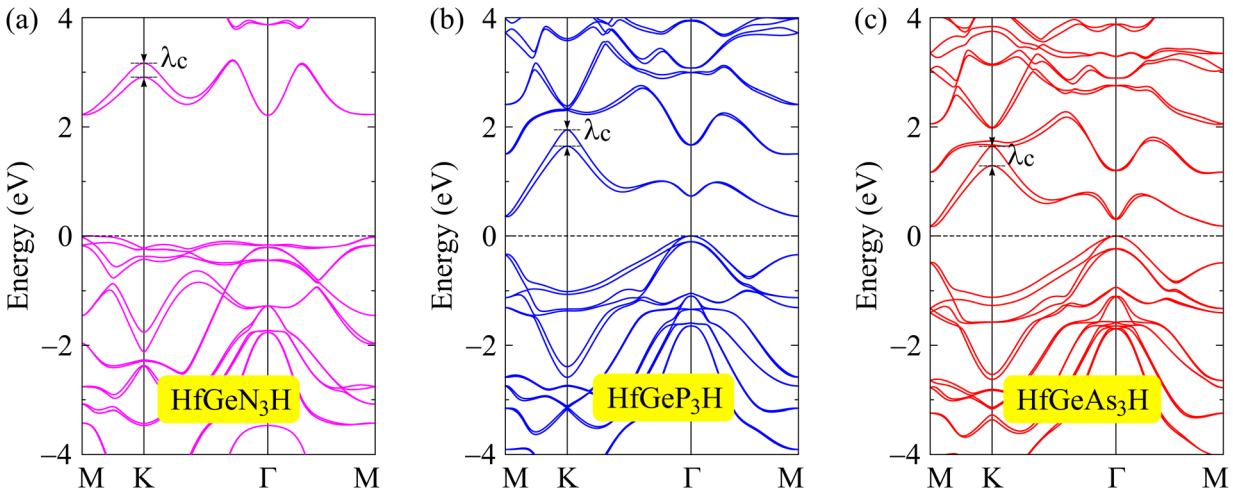

Fig. 4 Band structures computed by the PBE + SOC approach of (a) $HfGeN_3H$, (b) $HfGeP_3H$, and (c) $HfGeAs_3H$ monolayers.

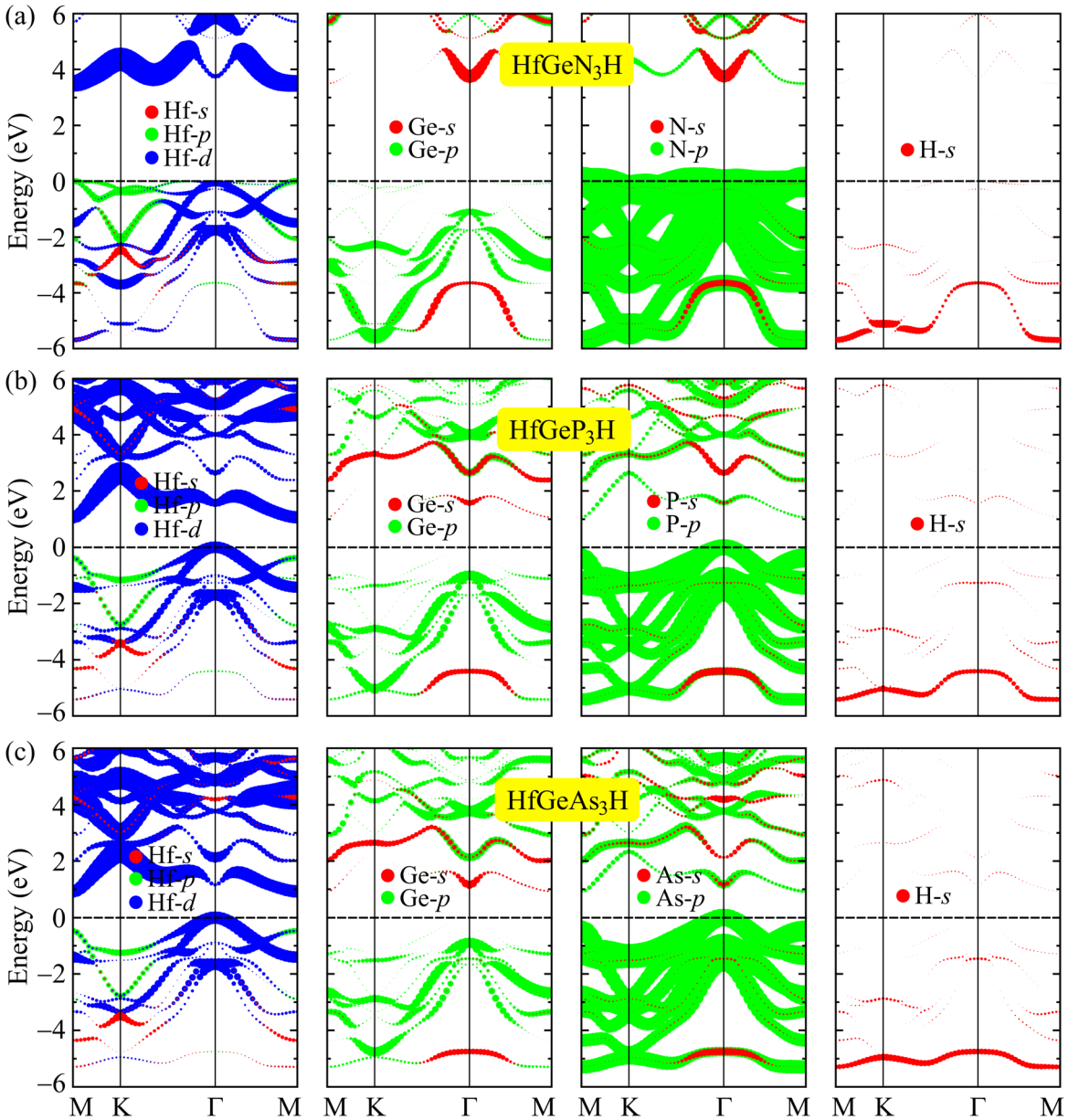

Fig. 5 The PBE weighted bands of (a) $HfGeN_3H$, (b) $HfGeP_3H$, and (c) $HfGeAs_3H$ monolayers.

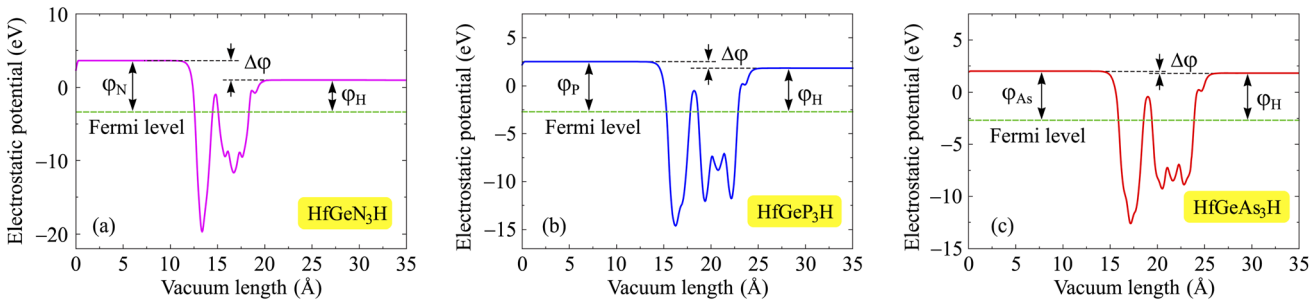

Fig. 6 Electrostatic potentials of (a) $HfGeN_3H$, (b) $HfGeP_3H$, and (c) $HfGeAs_3H$ monolayers.

Table 3 Elastic constants C_{ij} (N m^{-1}), Young's modulus Y_{2D} (N m^{-1}), Poisson's ratio ν, and piezoelectric coefficients e_{11} (10^{-10} C m^{-1}), e_{31} (10^{-10} C m^{-1}), d_{11} (pm V^{-1}), and d_{31} (pm V^{-1}) of Janus $HfGeZ_3H$

	C_{11}	C_{12}	C_{66}	Y_{2D}	ν	e_{11}	e_{31}	d_{11}	d_{31}
$HfGeN_3H$	274.66	100.87	86.89	237.61	0.37	2.77	0.32	1.59	0.09
$HfGeP_3H$	115.64	39.43	38.10	102.19	0.34	−0.65	0.14	−0.86	0.09
$HfGeAs_3H$	100.67	37.87	31.40	86.42	0.38	−1.12	0.02	−1.78	0.01

which is attributed to the structural asymmetry of Janus systems. Besides, because the sides of the Janus system are made up of different atoms, the vacuum levels on the two sides are also different, leading to unequal work functions on the two sides of the systems. It is calculated that the vacuum level difference $\Delta\varphi$ between the two sides decreases as the Z element changes from N to As. The computed values for $HfGeN_3H$, $HfGeP_3H$, and $HfGeAs_3H$ are 2.66, 0.68, and 0.19 eV, respectively. The obtained values of the vacuum level difference and the work function at the two surfaces of the Janus material are detailed in Table 3. The calculation results reveal that the work functions at the two sides for the three $HfGeZ_3H$ systems go from 2.68 to 3.36 eV. Indeed, the values for the work function and the vacuum level difference gradually decrease with the increasing atomic number of element Z. In each given Janus system, the work function at the H surface is smaller than that at the Z side. In other words, it is more difficult for electrons to escape from the Z surface than from the H one.

3.3 Piezoelectric effect

Piezoelectricity is a crucial property of materials that enables the transformation of mechanical energy into electrical energy or *vice versa*. A piezoelectric semiconductor is subject to significant limitations due to its crystalline symmetry. The occurrence of piezoelectric effects is limited to structures that lack centrosymmetry. The piezoelectric features of $HFGeZ_3H$ materials can be attributed to their noncentrosymmetry, resulting in both in-plane and out-of-plane piezoelectric effects. Recent experimental measurements show good agreement between experimental results[25] and previous DFT calculations[6] for piezoelectric coefficients in 2D MoS_2 monolayers. Piezoelectricity refers to the ground-state characteristics that are strongly associated with polarization. Therefore, DFT calculations have been demonstrated to be a reliable method for predicting piezoelectric coefficients.

Initially, we compute the elastic stiffness coefficients C_{ij}, which are essential for determining the piezoelectric coefficients. Based on C_{ij}, we can also evaluate the elastic stability as well as the basic mechanical characteristics of the material. The elastic stiffness coefficients C_{ij} are determined using the energy–strain relationships. Here, the relaxed-ion coefficients, whose positions of the atoms were relaxed at each value of strain, are calculated. The relaxed-ion coefficients are anticipated to exhibit greater consistency with experimental measurements than the clamped-ion coefficients.[6] Table 2 summarizes our calculated results for the relaxed-ion elastic constants C_{11}, C_{12}, and C_{66}. Importantly, the obtained values of C_{ij} for $HfGeZ_3H$ satisfy the criterion for mechanical stabilities proposed by Born and Huang in 2D materials ($C_{11} > 0$ and ${C_{11}}^2 - {C_{12}}^2 > 0$),[50,51] ensuring that our predicted Janus monolayers are mechanically stable. Based on the results of these elastic constants, we obtain Young's modulus Y_{2D} and Poisson's ratio ν as follows:

$$Y_{2D} = \frac{{C_{11}}^2 - {C_{12}}^2}{C_{11}}, \tag{2}$$

$$\nu = \frac{C_{12}}{C_{11}}. \tag{3}$$

Our results show that Janus compounds $HfGeZ_3H$ possess isotropic mechanical properties, which are attributed to their isotropic structure. Table 2 reveals that the Young's modulii of $HfGeN_3H$, $HfGeP_3H$, and $HfGeAs_3H$ are 237.61, 102.19, and 86.42 N m^{-1}, respectively. Young's modulus of $HfGeZ_3H$ is comparable to that of $MoGeZ_3H$;[52] however, it is much smaller than that of graphene.[53] It reflects that $HfGeZ_3H$ monolayers are predicted to be mechanically flexible structures.

The modern theory of polarization has revealed that the change in polarization e_{ijk} when uniaxial strain is applied is the basis for evaluating the linear piezoelectric coefficient d_{ijk}.[54] In 2D materials, the linear piezoelectric effect may be understood as a first-order coupling between the surface polarization (P_i) and the strain (ε_{jk}) or stress (σ_{jk}) tensors. Here, $i, j, k \in \{1, 2, 3\}$ and 1, 2, and 3 correspond respectively to x, y, and z.

The piezoelectric tensors e_{ijk} and d_{ijk} are third-rank tensors, which are evaluated according to the following expression:[6]

$$e_{ijk} = \frac{\partial P_i}{\partial \varepsilon_{jk}}, \tag{4}$$

$$d_{ijk} = \frac{\partial P_i}{\partial \sigma_{jk}}. \tag{5}$$

The crystallographic symmetry element is used to determine the degree of piezoelectric response in 2D materials. In the case of Janus asymmetric $HfGeZ_3H$, which belongs to the point symmetry group $P3m1$, it simultaneously possesses in-plane (e_{11}) and out-of-plane (e_{31}) piezoelectric coefficients. We can calculate e_{11} and e_{31} by introducing uniaxial strain along the x axis of the orthorhombic supercell using the density functional perturbation theory. The coefficients d_{ij} are then calculated according to the expression:[28]

$$d_{11} = \frac{e_{11}}{C_{11} - C_{12}}, \tag{6}$$

$$d_{31} = \frac{e_{31}}{C_{11} + C_{12}}. \quad (7)$$

Table 2 presents the computed results of the piezoelectric coefficients of $HfGeZ_3ZH$. The piezoelectric coefficient e_{11} is the largest in the Janus $HfGeN_3H$ monolayer (2.77×10^{-10} C m^{-1}), while the magnitude of d_{11} is the largest in the $HfGeAs_3H$ monolayer (-1.78 pm V^{-1}). These values are smaller than the corresponding piezoelectric coefficients in structurally similar compounds such as $MoGeZ_3H$[55] and $WSiZ_3H$.[56] More importantly, the out-of-plane piezoelectric coefficients in Janus structures are non-zero, resulting from the breaking of mirror symmetry due to different atoms at the two surfaces of the material. Specifically, the values of e_{31} are 0.32×10^{-10}, 0.14×10^{-10}, and 0.02×10^{-10} C m^{-1} for the $HfGeN_3H$, $HfGeP_3H$, and $HfGeAs_3H$ monolayers, respectively. These results reflect that the $HfGeN_3H$ monolayer has the highest e_{31} among the studied monolayers, which is comparable to that of similar Janus structures such as $MoGeZ_3H$[55] and $WSiZ_3H$.[56] In addition, the out-of-plane piezoelectricity d_{31} of $HfGeZ_3H$ monolayers has a value ranging from 0.01 to 0.09 pm V^{-1}. The obtained values of d_{31} are close to that in the Janus $WSiZ_3H$ monolayer.[56] The above results reveal that 2D Janus $HfGeZ_3H$ systems are suitable for piezoelectric applications.

3.4 Carrier mobility

2D semiconductors with high carrier mobility offer great potential for high-speed nanoelectronics. In the last section, we investigate mobilities of carriers (electron/hole) of Janus $HfGeZ_3H$ using the deformation potential (DP) theory suggested by Bardeen and Shockley.[47] The carrier mobility μ_{2D} for a 2D nanostructure is written as:[57]

$$\mu_{2D} = \frac{e\hbar^3 C_{2D}}{k_B T m^* \overline{m}^* E_l^2}, \quad (8)$$

where e denotes the electron charge, k_B is the Boltzmann's constant, and $\hbar$ is the reduced Plank's constant. m^* is the effective mass and the average effective mass is given by $\overline{m} = \sqrt{m_x m_y}$. The temperature is marked by T. C_{2D} denotes the elastic modulus and E_l refers to the DP constant. The rectangular supercell is chosen to calculate the carrier mobilities of the studied structures with $T = 300$ K.

The effective mass m^*, elastic modulus C_{2D}, and DP constant E_l are defined using

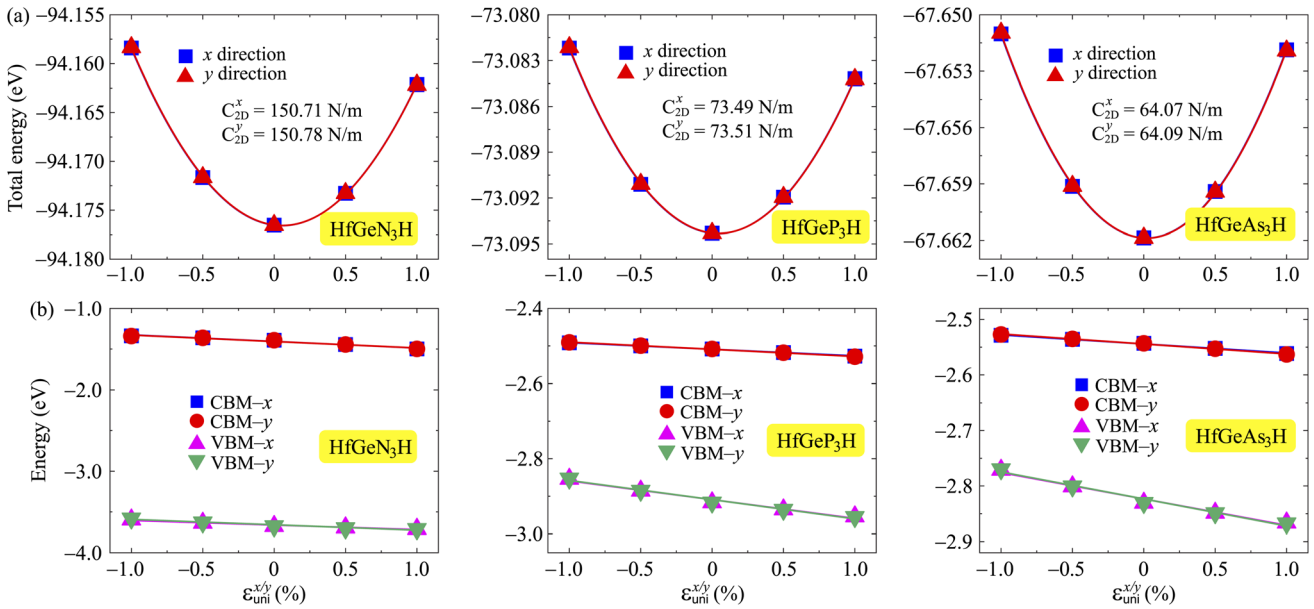

Fig. 7 (a) The total energy shifting and (b) positions of the CBM/VBM in $HfGeZ_3H$ monolayers as functions of the uniaxial strain $\varepsilon_{uni}^{x/y}$.

Table 4 Computed effective mass of carriers m^* (in units of mass of a free electron m_0), 2D elastic modulus C_{2D} (N m^{-1}), DP constant E_l (eV), and mobility of carriers μ (cm^2 V^{-1} s^{-1}) of $HfGeZ_3H$ along the x/y transport directions

		m_x^*	m_y^*	$C_{2D}{}^x$	$C_{2D}{}^y$	$E_l{}^x$	$E_l{}^y$	μ_x	μ_y
Electron	$HfGeN_3H$	2.49	1.38	150.71	150.78	−8.09	−7.96	10.65	19.84
	$HfGeP_3H$	0.23	0.53	73.49	73.51	−1.77	−1.90	6.26×10^3	2.35×10^3
	$HfGeAs_3H$	0.23	0.53	64.07	64.09	−1.64	−1.80	6.40×10^3	2.31×10^3
Hole	$HfGeN_3H$	1.48	2.26	150.71	150.78	−5.69	−6.62	36.77	17.69
	$HfGeP_3H$	0.82	0.90	73.49	73.51	−5.01	−5.12	89.07	76.92
	$HfGeAs_3H$	0.77	0.83	64.09	64.09	−4.76	−4.87	97.35	86.88

$$\frac{1}{m^*} = \frac{1}{\hbar^2}\left|\frac{\partial^2 E(K)}{\partial k^2}\right|, \quad (9)$$

$$C_{2D} = \frac{1}{\Omega_0}\frac{\partial^2 E_{tot}}{\partial {\varepsilon_{uni}}^2}, \quad (10)$$

$$E_d = \frac{\Delta E_{edge}}{\varepsilon_{uni}}, \quad (11)$$

where $E(k)$ is the dispersion at the band edges, Ω_0 refers to the area of the optimized unitcell, E_{tot} indicates the total energy, ΔE_{edge} refers to the change in band-edge energy referencing to the vacuum level, and ε_{uni} denotes the uniaxial strain applied along the examined transport directions (x/y).

It is demonstrated that the effective masses of electrons in $HfGeP_3H$ and $HfGeAs_3H$ monolayers are small, indicating that they exhibit high electron mobility. The effective mass of electrons along the x direction m_x^{*e} is found to be $0.23m_0$ (m_0 is the free electron mass) for both $HfGeP_3H$ and $HfGeAs_3H$ monolayers. Meanwhile, the values of m_x^{*e} and m_y^{*e} for $HfGeN_3H$ are calculated to be $2.49m_0$ and $1.38m_0$, respectively. This is because the radius of curvature of dispersion around the CBM of $HfGeN_3H$ is larger than that of $HfGeP_3H$ and $HfGeAs_3H$. The larger the radius of curvature (the flatter the dispersion), the larger the effective mass because the effective mass is inversely proportional to $\partial^2 E(k)/\partial k^2$ as written in eqn (9). Fig. 7 shows the uniaxial strain-dependence of the total energy and band-edge positions in $HfGeZ_3H$ monolayers. From Fig. 7, we can see that both C_{2D} and E_l exhibit quite directionally isotropic along the two transport axes. The calculated results for the transport parameters, including carrier mobilities, of $HfGeZ_3H$ monolayers are tabulated in Table 4. Our results reveal that the electron and hole mobilities exhibit directional anisotropy because the values of μ_e and μ_h are different along the x and y directions. This is mainly due to the directional anisotropy of effective mass as mentioned above. As revealed in Table 4, $HfGeZ_3H$ monolayers exhibit low hole mobility, ranging from 17.69 to 97.35 $cm^2\ V^{-1}\ s^{-1}$. Meanwhile, due to the low electron effective mass, both $HfGeP_3H$ and $HfGeAs_3H$ have ultra-high electron mobility, up to $6.40 \times 10^3\ cm^2\ V^{-1}\ s^{-1}$. This suggests that $HfGeP_3H$ and $HfGeAs_3H$ monolayers are excellent candidates for applications in electronic devices due to their high electron mobility.

4 Conclusive remarks

The structural stabilities and basic physical properties of 2D Janus $HfGeZ_3H$ (Z = N, P, As) monolayers were theoretically studied based on the first-principles method. Janus $HfGeZ_3H$ monolayers are predicted to be energetically, dynamically, and mechanically stable. Our first-principles simulations demonstrated that $HfGeZ_3H$ monolayers are all semiconductors with high electron mobilities up to $6.40 \times 10^3\ cm^2\ V^{-1}\ s^{-1}$. The influences of the SOC on the band diagrams of $HfGeZ_3H$ are significant; in particular, a spin-splitting energy of up to 0.36 eV has been observed in Janus $HfGeAs_3H$ monolayers. Besides the in-plane piezoelectric effect, vertical polarization due to the symmetry breaking in Janus $HfGeZ_3H$ gives rise to out-of-plane piezoelectric responses with d_{31} ranging from 0.01 to 0.09 pm V^{-1}. Janus $HfGeZ_3H$ monolayers can be proposed for various applications due to their versatile electronic features, high electron mobility, and strong piezoelectric response.

Data availability

All data that support the findings of this study are included within the article.

Conflicts of interest

There are no conflicts of interest to declare.

Acknowledgements

This work was supported by Hue University under project number DHH2023-04-207.

References

1 X. Wang, J. Zhou, J. Song, J. Liu, N. Xu and Z. L. Wang, *Nano Lett.*, 2006, **6**, 2768–2772.
2 M. Lanza, M. Reguant, G. Zou, P. Lv, H. Li, R. Chin, H. Liang, D. Yu, Y. Zhang, Z. Liu and H. Duan, *Adv. Mater. Interfaces*, 2014, **1**, 1300101.
3 M. Yuan, L. Cheng, Q. Xu, W. Wu, S. Bai, L. Gu, Z. Wang, J. Lu, H. Li, Y. Qin, T. Jing and Z. L. Wang, *Adv. Mater.*, 2014, **26**, 7432–7437.
4 J. Xin, Y. Zheng and E. Shi, *Appl. Phys. Lett.*, 2007, **91**, 112902.
5 M. N. Blonsky, H. L. Zhuang, A. K. Singh and R. G. Hennig, *ACS Nano*, 2015, **9**, 9885–9891.
6 K.-A. N. Duerloo, M. T. Ong and E. J. Reed, *J. Phys. Chem. Lett.*, 2012, **3**, 2871–2876.
7 A.-Y. Lu, H. Zhu, J. Xiao, C.-P. Chuu, Y. Han, M.-H. Chiu, C.-C. Cheng, C.-W. Yang, K.-H. Wei, Y. Yang, Y. Wang, D. Sokaras, D. Nordlund, P. Yang, D. A. Muller, M.-Y. Chou, X. Zhang and L.-J. Li, *Nat. Nanotechnol.*, 2017, **12**, 744.
8 J. Zhang, S. Jia, I. Kholmanov, L. Dong, D. Er, W. Chen, H. Guo, Z. Jin, V. B. Shenoy, L. Shi and J. Lou, *ACS Nano*, 2017, **11**, 8192–8198.
9 Y. Zhu, Z. Qu, J. Zhang, X. Wang, S. Jiang, Z. Xu, F. Yang, Z. Wu and Y. Dai, *Phys. Chem. Chem. Phys.*, 2024, **26**, 4555–4563.
10 T. V. Vu, V. T. T. Vi, H. V. Phuc, A. I. Kartamyshev and N. N. Hieu, *Phys. Rev. B*, 2021, **104**, 115410.
11 N. N. Hieu, H. V. Phuc, A. I. Kartamyshev and T. V. Vu, *Phys. Rev. B*, 2022, **105**, 075402.
12 T. Zhang, Y. Liang, H. Guo, H. Fan and X. Tian, *Appl. Surf. Sci.*, 2022, **579**, 152017.
13 N. Ghobadi, S. Gholami Rudi and S. Soleimani-Amiri, *Phys. Rev. B*, 2023, **107**, 075443.
14 N. T. Hiep, C. Q. Nguyen and N. N. Hieu, *Appl. Phys. Lett.*, 2023, **123**, 092102.

15 D. Bezzerga, E.-A. Haidar, C. Stampfl, A. Mir and M. Sahnoun, *Nanoscale Adv.*, 2023, **5**, 1425–1432.
16 T. V. Vu, H. V. Phuc, A. I. Kartamyshev and N. N. Hieu, *Appl. Phys. Lett.*, 2023, **122**, 061601.
17 Y. Zhang, Y. Shen, J. Liu, L. Lv, M. Zhou, X. Yang, X. Meng, B. Zhang and Z. Zhou, *Phys. Chem. Chem. Phys.*, 2023, **25**, 22889–22899.
18 B. Akgenc, E. Vatansever and F. Ersan, *Phys. Rev. Mater.*, 2021, **5**, 083403.
19 D. H. Ozbey, M. E. Kilic and E. Durgun, *Phys. Rev. Appl.*, 2022, **17**, 034043.
20 B. Akgenc, *Comput. Mater. Sci.*, 2020, **171**, 109231.
21 A. Kaur, S. Sharma, P. Nandi and A. De Sarkar, *Phys. E*, 2023, **154**, 115791.
22 N. Tripathy and A. De Sarkar, *J. Phys.: Condens.Matter*, 2023, **35**, 335301.
23 H.-N. Zhang, Y. Wu, C. Yang, L.-H. Zhu and X.-C. Wang, *Phys. Rev. B*, 2021, **104**, 235437.
24 Y.-Q. Li, X.-Y. Wang, S.-Y. Zhu, D.-S. Tang, Q.-W. He and X.-C. Wang, *J. Phys. Chem. Lett.*, 2022, **13**, 9654–9663.
25 H. Zhu, Y. Wang, J. Xiao, M. Liu, S. Xiong, Z. J. Wong, Z. Ye, Y. Ye, X. Yin and X. Zhang, *Nat. Nanotechnol.*, 2014, **10**, 151–155.
26 W. Wu, L. Wang, Y. Li, F. Zhang, L. Lin, S. Niu, D. Chenet, X. Zhang, Y. Hao, T. F. Heinz, J. Hone and Z. L. Wang, *Nature*, 2014, **514**, 470–474.
27 R. Fei, W. Li, J. Li and L. Yang, *Appl. Phys. Lett.*, 2015, **107**, 173104.
28 Y. Guo, S. Zhou, Y. Bai and J. Zhao, *Appl. Phys. Lett.*, 2017, **110**, 163102.
29 T. V. Vu, H. V. Phuc, A. I. Kartamyshev and N. N. Hieu, *Appl. Phys. Lett.*, 2023, **122**, 061601.
30 T. V. Vu, B. D. Hoi, A. I. Kartamyshev and N. N. Hieu, *J. Appl. Phys.*, 2024, **135**, 074301.
31 Y.-L. Hong, Z. Liu, L. Wang, T. Zhou, W. Ma, C. Xu, S. Feng, L. Chen, M.-L. Chen, D.-M. Sun, X.-Q. Chen, H.-M. Cheng and W. Ren, *Science*, 2020, **369**, 670–674.
32 L. Wang, Y. Shi, M. Liu, A. Zhang, Y.-L. Hong, R. Li, Q. Gao, M. Chen, W. Ren, H.-M. Cheng, Y. Li and X.-Q. Chen, *Nat. Commun.*, 2021, **12**, 2361.
33 R. Sibatov, R. Meftakhutdinov and A. Kochaev, *Appl. Surf. Sci.*, 2022, **585**, 152465.
34 N. T. Hiep, N. P. Q. Anh, H. V. Phuc, C. Q. Nguyen, N. N. Hieu and V. T. T. Vi, *Phys. Chem. Chem. Phys.*, 2023, **25**, 8779–8788.
35 H. T. Nguyen, N. Q. Cuong, V. T. T. Vi, N. N. Hieu and L. P. T. Tran, *Phys. Chem. Chem. Phys.*, 2023, **25**, 21468–21478.
36 N. P. Q. Anh, N. T. Hiep, D. V. Lu, C. Q. Nguyen, N. N. Hieu and V. T. T. Vi, *Nanoscale Adv.*, 2023, **5**, 6705–6713.
37 T. V. Vu, H. V. Phuc, C. V. Nguyen, V. T. T. Vi, A. I. Kartamyshev and N. N. Hieu, *Phys. Chem. Chem. Phys.*, 2022, **24**, 16512–16521.
38 G. Kresse and J. Furthmüller, *Phys. Rev. B: Condens. Matter Mater. Phys.*, 1996, **54**, 11169–11186.
39 G. Kresse and J. Furthmüller, *Comput. Mater. Sci.*, 1996, **6**, 15–50.
40 P. E. Blöchl, *Phys. Rev. B: Condens. Matter Mater. Phys.*, 1994, **50**, 17953.
41 G. Kresse and D. Joubert, *Phys. Rev. B: Condens. Matter Mater. Phys.*, 1999, **59**, 1758–1775.
42 J. P. Perdew, K. Burke and M. Ernzerhof, *Phys. Rev. Lett.*, 1996, **77**, 3865.
43 J. Heyd, G. E. Scuseria and M. Ernzerhof, *J. Chem. Phys.*, 2003, **118**, 8207.
44 S. Grimme, J. Antony, S. Ehrlich and H. Krieg, *J. Chem. Phys.*, 2010, **132**, 154104.
45 A. H. MacDonald, W. E. Picket and D. D. Koelling, *J. Phys. C: Solid State Phys.*, 1980, **13**, 2675.
46 A. Togo, L. Chaput and I. Tanaka, *Phys. Rev. B: Condens. Matter Mater. Phys.*, 2015, **91**, 094306.
47 J. Bardeen and W. Shockley, *Phys. Rev.*, 1950, **80**, 72.
48 J. P. Perdew and M. Levy, *Phys. Rev. Lett.*, 1983, **51**, 1884–1887.
49 L. Hedin, *Phys. Rev.*, 1965, **139**, A796.
50 M. Born and K. Huang, *Am. J. Physiol.*, 1955, **23**, 474.
51 R. C. Andrew, R. E. Mapasha, A. M. Ukpong and N. Chetty, *Phys. Rev. B: Condens. Matter Mater. Phys.*, 2012, **85**, 125428.
52 X. Cai, G. Chen, R. Li, W. Yu, X. Yang and Y. Jia, *Phys. Chem. Chem. Phys.*, 2023, **25**, 29594–29602.
53 C. Lee, X. Wei, J. W. Kysar and J. Hone, *Science*, 2008, **321**, 385–388.
54 R. D. King-Smith and D. Vanderbilt, *Phys. Rev. B: Condens. Matter Mater. Phys.*, 1993, **47**, 1651–1654.
55 X. Cai, G. Chen, R. Li, Z. Pan and Y. Jia, *J. Mater. Chem. C*, 2024, **12**, 4682.
56 T. V. Vu, B. D. Hoi, A. I. Kartamyshev and N. N. Hieu, *J. Appl. Phys.*, 2024, **135**, 074301.
57 S.-D. Guo, W.-Q. Mu, Y.-T. Zhu, R.-Y. Han and W.-C. Ren, *J. Mater. Chem. C*, 2021, **9**, 2464–2473.